Optical cavities and quantum emitters
Koks, C.

Citation
Koks, C. (2024, January 25). *Optical cavities and quantum emitters*. *Casimir PhD Series*. Retrieved from https://hdl.handle.net/1887/3715075

Version:	Publisher's Version
License:	[Licence agreement concerning inclusion of doctoral thesis in the Institutional Repository of the University of Leiden](#)
Downloaded from:	https://hdl.handle.net/1887/3715075

Note: To cite this publication please use the final published version (if applicable).

7

EXPLORING POLARIZATION ORIENTATION AND POWER-DEPENDENT DYNAMICS OF SINGLE-PHOTON EMITTERS IN HEXAGONAL BORON NITRIDE

Single-photon emitters in a hexagonal Boron Nitride flake are investigated with a confocal microscope. Two very stable emitters are identified, both exhibiting well-defined excitation and emission dipoles that are shifted approximately 10 degrees. To confirm that these are single-photon emitters, photon correlation measurements are conducted, also revealing two distinctive bunching times spanning from hundreds of nanoseconds to nearly a millisecond. A decrease in both bunching times is observed as the excitation power increases, a phenomenon that can be explained by a four-level system featuring power-dependent rates. Two distinct models for the dynamics are presented, suggesting the presence of processes involving two-photon absorption. The investigation of these emitters sheds light on their precise origin and provides valuable insights into their dynamics.

C. Koks, M. Fischer, N. Stenger and M. P. van Exter (to be submitted)

7.1. INTRODUCTION

Single-photon emitters play a crucial role in the development of the quantum internet [1]. They can be generated using various systems, such as quantum dots [11, 29], trapped ions [117], or spontaneous parametric down-conversion in various crystals [118]. Hexagonal Boron Nitride (hBN) also hosts room-temperature single-photon emitters [119]. Some of these emitters have a magnetic resonance response similar to NV centers in diamond [120, 121], offering sensitive magnetic field sensing capabilities. When coupled with microcavities, their emission can be enhanced [50, 77], enabling applications in quantum communication [122].

Variability in hBN-based single-photon emitters remains a subject of ongoing debate. It has been proposed that some emitters originate from a carbon atom that replaced the nitrogen or boron atoms [35, 36]. It has also been suggested that some emitters are just residual polymers from the fabrication process [37]. The emitters in the flake studied in this chapter originate from defects created by oxygen-ion irradiation and could be explained with DFT studies [123]. Precise measurements of other aspects of the emitter, besides the emission spectrum [124] may lead to a deeper theoretical understanding of the origin of these emitters [125].

In this chapter, we investigate several selected emitters in hBN flakes. The initial focus is on emitter identification through co-linear polarization scans. Subsequently, we determine the orientation of the excitation and emission dipoles, revealing a slight angle between them. Further, we explore the power dependence of the second-order autocorrelation function $g^2(\tau)$, which uncovers dynamics spanning several orders of magnitude. We propose two different four-level models with power-dependent transition rates to explain the observed dynamics.

7.2. EXPERIMENTAL SETUP

The measurements are conducted with a home-built confocal microscope setup, shown in figure 7.1. The hBN flakes, placed on a DBR mirror, are non-resonantly excited with a laser at $\lambda = 532$ nm (Innolight Prometheus). This laser light is coupled via a single-mode fiber and then outcoupled with a 20x objective, using an additional 532 nm bandpass filter to suppress any excess fluorescence from the optical fiber. A dichroic mirror ($\lambda_{\text{cutoff}} = 520$ nm at 45 degrees) effectively separates the excitation and emission beams. To adjust the cutoff wavelength to around 540 nm, the excitation laser is angled at approximately 40 degrees relative to the dichroic mirror. A 100x apochromatic objective (NA = 0.9) focuses the excitation laser onto the hBN flakes on an XYZ-piezo stack. The fluorescence from the sample is collected into a different single-mode fiber, which is linked either to a fiber beam splitter attached to two single-photon counting modules (SPCM), which collects all light between $\lambda = 550 - 1050$ nm, or to a spectrometer.
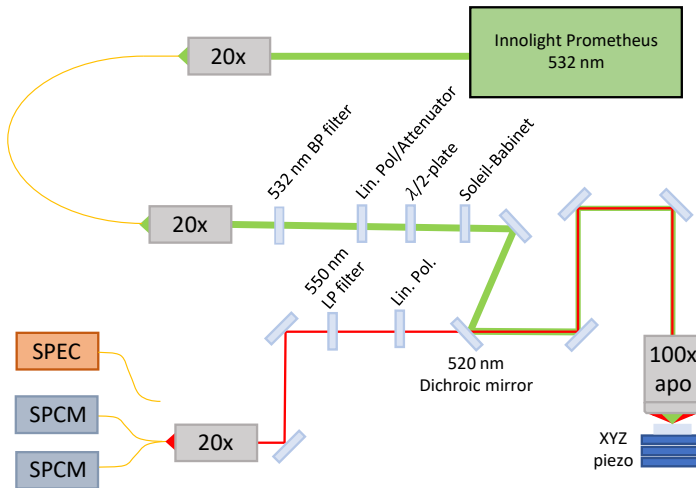

Figure 7.1: Schematic image of the experimental setup. The excitation laser (green) is focused onto a sample on an XYZ-piezo stage. The fluorescence from the sample (red) passes through a dichroic mirror and is fiber-coupled, either to a fiber beam splitter and two SPCMs, or a spectrometer (SPEC). The setup includes spectral filters and polarization optics (see main text).

The setup allows precise determination of the excitation and emission dipole orientation for the emitters on the sample. The excitation dipole is controlled using a $\lambda/2$-plate,

positioned just after a liquid-crystal attenuator which acts as a linear polarizer. To compensate for the reflection phase difference of the dichroic mirror for s- and p-polarized light, we use a Soleil-Babinet compensator and tune it such that its phase difference is precisely opposite of that of the dichroic mirror. The emission dipole is determined by using a linear polarizer in the detection path. The dichroic mirror has (almost) no effect on the phase in transmission and therefore requires no compensation. To mitigate ellipticity and wavelength-dependent effects, metallic instead of dielectric mirrors are employed throughout the setup. The accuracy of polarization control was determined through calibration using a linear polarizer placed in the beam path just above the 100x objective. By measuring the transmission at different settings—horizontal, vertical, diagonal, and antidiagonal—we find that the dipole orientation can be determined with an accuracy better than 1 degree.

The sample, provided by the Technical University of Denmark, comprises several hBN flakes, which were irradiated with oxygen ions followed by an annealing step at 850 °C in nitrogen [123]. Calculations and measurements reported in ref. [38] suggest that the studied single emitters are most likely C_2C_B, C_2C_N or V_NC_B defects. The substrate is a highly reflective DBR mirror with a stopband between 580 and 660 nm. The reflection phase of the mirror is such that the anti-node is between 0 nm and 60 nm above the surface for wavelengths between $\lambda \approx 580$ to 600 nm.
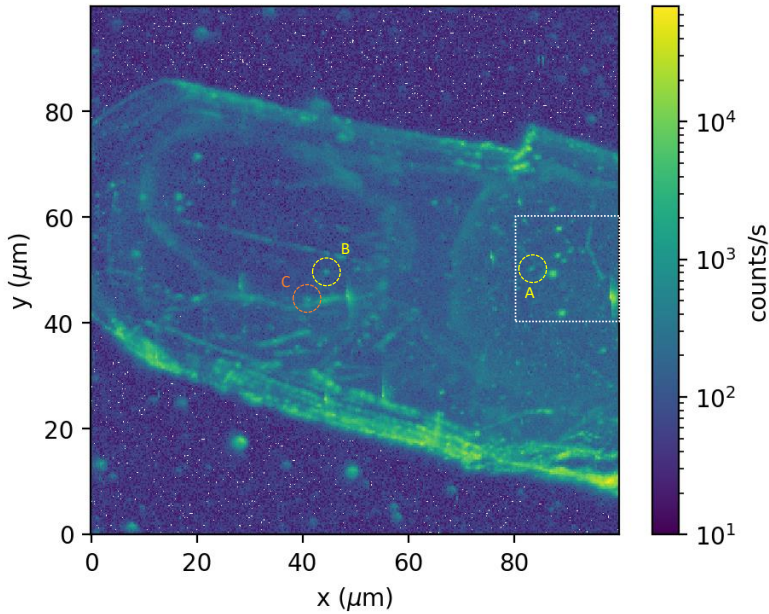

Figure 7.2: Fluorescence map ($\lambda_{emit} = 550 - 1100$ nm) of the studied hBN flake at $P = 800$ μW. The yellow circles indicate the very stable emitters A and B, the orange circle indicates the almost stable emitter C. A zoom-in of the white box is shown in figure 7.3a.

7.3. Confocal scan of the emitters

Figure 7.2 shows a confocal scan of (part of) the flake. The scan shows several bright lines across the flake which may be small cracks. Such "lines" are not continuous lines but consist of separate hotspots of fluorescence (see also figure 7.3a). Hanbury-Brown and Twiss measurements show that these hotspots are not single-photon emitters. Our primary focus lies in single-photon emitters that are not positioned at the flake's edges or lines. Three such emitters are encircled in the figure, which below shall be referred to as emitters A, B, and C.

Figure 7.3a shows a more detailed XY-scan of the white box in figure 7.2. On top of each pixel, a small black loop is plotted to show the angular emission dependence in a "colinear" polarization scan, with identical excitation and emission polarization. A perfect circle indicates no polarization dependence, whereas a $\cos^2(\theta)$-like shape indicates a potential single-photon emitter. Note that this colinear scan is not the same as a full polarization scan where the excitation and emission dipoles can be determined individually, as in figure 7.4 below.

Figure 7.3a shows several bright centers. These centers can be categorized into three different groups based on the time before they bleach: (i) unstable, (ii) almost stable, and (iii) very stable. (i) Unstable emitters are the most common. Emitters like the one at $x = 98$ μm, $y = 45$ μm are typically very bright but show gradual bleaching, visible as an inward-spiral in Fig. 7.3. The gradual bleaching indicates that these are not single-photon emitters. (ii) Almost stable emitters show a $\cos(\theta)^2$-like behavior in their angular emission dependence, like for example the emitter in $x = 83$ μm, $y = 45$ μm in Fig. 7.3. Although less common than (i), we still find 4 of such emitters in the 20x20 μm^2 area in Fig. 7.3. Almost stable emitters bleach with time scales ranging from half an hour to 2 hours when operating at their saturation power. Measurements on one such an emitter are shown in Appendix 7.C. (iii) Very stable emitters are rare. We could only identify 2 of such emitters over the full flake, as Fig. 7.2 shows. These emitters show prominent $\cos(\theta)^2$-like behavior and are stable for more than 10 hours at saturation power. The emitters in the third category, labeled as A and B, are the main focus of this study.

Figures 7.3b and 7.3c display the saturation curve and spectrum of the very stable emitter A. The saturation curve is fitted with the equation $I = I_\infty/(1 + P/P_{\text{sat}})$, yielding parameters $I_\infty = 6.38(5)$ kCounts/s and $P_{\text{sat}} = 74(2)$ μW. Notably, these counts are measured behind a fiber beam splitter, accounting for approximately a one-third reduction in counts due to the beam splitter and fiber coupler losses. Adjusting for this factor, the saturated count rate is approximately 20 kCounts/s, similar to the defects reported in [18]. The corresponding spectrum in Fig. 7.3 reveals a zero-phonon-line situated at 580.3(5) nm, accompanied by a phonon sideband positioned at 637(1) nm. The resulting separation of 190(2) meV is comparable to the 180 meV reported in [123].

7.4. Dipole orientation

Figure 7.4 shows the fluorescence counts as a function of the angles of the emission and excitation polarization for emitters A and B. The measurements are performed well below the saturation power at $P \approx 0.2 P_{\text{sat}}$ for the optimal excitation angle. The angles of the excitation and emission are rotated independently from 0 to 360 degrees in 40 steps, where at each emission angle, the excitation angle is rotated a full 360 degrees. The resulting steps
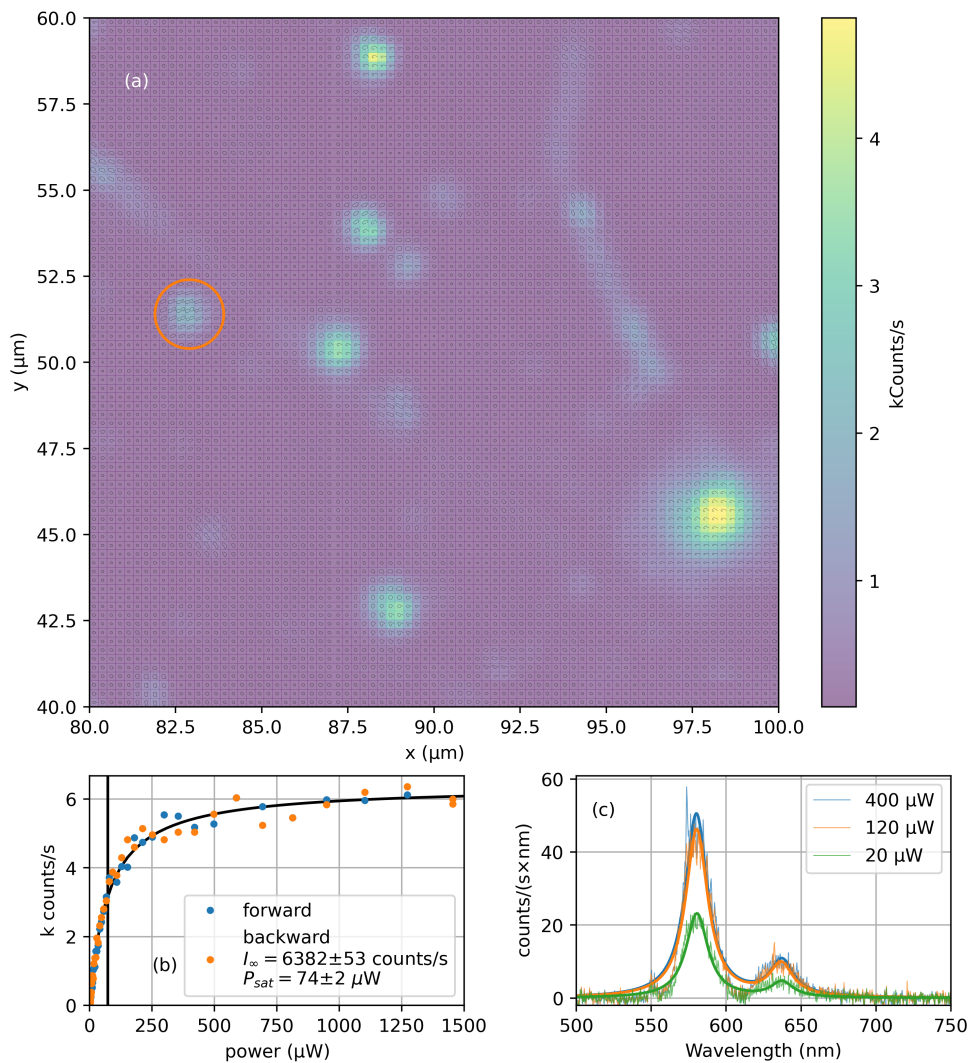
Figure 7.3: (a) Intensity and polarization map of photon emitters in a hBN flake, over the spectral range $\lambda = 550 - 1100$ nm. On top of each pixel, a small black loop is plotted (better visible when zooming in on the figure in the digital version). This loop shows the angle-dependent emission in polar coordinates for a colinear polarization scan. The false colors indicate the counts at the optimal polarization angle. A Gaussian filter with a width of 0.25 μm is used to improve the image quality. Additional measurements on the yellow encircled emitter A: (b) saturation curve and (c) emission spectrum at three different excitation powers, including a fit with two lorentzians.

of 9° are small enough to accurately determine the dipole orientations, but large enough to limit the total scan time. The counts in Fig. 7.4 are the sum of the counts for all emission (excitation) angles at a fixed excitation (emission) angle. During these ~30-minute scans, both emitter A and B suffer from a slight drift in the XY-position. This is most prominently visible in the measurement of the emission angle since this is the slow-varying parameter in the scan. The counts for the angular emission dependence are corrected for a slight linear decrease in counts, based on the difference between the first and last point.

The fit values show a difference between the excitation and emission dipoles $\Delta\phi = 11(1)°$ for emitter A, and $\Delta\phi = 9(1)°$ for emitter B. When the data is not corrected for a linear drift, the fitted emission-dipole orientations yield $\Delta\phi = 12(1)°$ for emitter A, and $\Delta\phi = 13(1)°$ for emitter B, which shows that the drift has only a slight influence on angles. We also measure that the degree of polarization of the excitation dipole is significantly smaller than that of the emission dipole. This might be caused by a difference in the emission dipole of the zero-phonon-line and the first-phonon-line (see Fig. 7.3c). Similar results were reported in ref. [124], which even links the measured dipole orientations to the crystal axes.
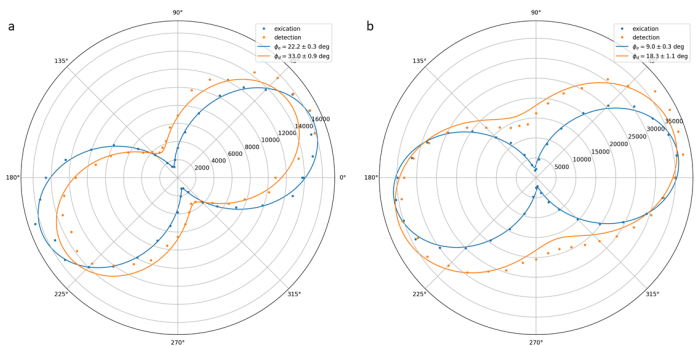

Figure 7.4: Fluorescence counts ($\lambda_{\text{emit}} = 550 - 1100$ nm) as a function of the excitation (blue) and emission (orange) polarization angles for (a) emitter A, and (b) emitter B. The points are fitted with a $\cos^2(\theta)$-relation with an offset. The fit does not fully match the measured values due to drift in the system (see text for details).

7.5. Blinking at two time scales

Figure 7.5 shows the second-order autocorrelation function measured for emitter B at various powers (dynamics of emitter A is shown in Appendix 7.B.). For the lowest power, the dip $g^2(0) = 0.12(2)$ indicates that this is indeed a single-photon emitter. At higher powers, the dip sharpens up and becomes less deep, being more limited by the (300 ps) jitter of the detectors [126]. The autocorrelation function at higher powers shows a clear bunching behavior. Two distinct "kinks" show up in these curves, corresponding to two different bunching processes. Therefore, based on ref. [126], we fit the graphs with three exponents;

$$g^2(\tau) = 1 - (1 + B + C)e^{-|\tau|/\tau_1} + Be^{-|\tau|/\tau_2} + Ce^{-|\tau|/\tau_3}, \qquad (7.1)$$

where the dip at zero delay $\tau = 0$ is set to be zero, i.e. $g^2(0) = 0$ for simplicity. τ_1 is the decay time of the dip, and τ_2 and τ_3 are two bunching time scales, with bunching amplitudes B and C. The measurements were performed in order of increasing power, where each measurement took about 1 hour (2 hours at the lowest power). The emitter bleached during the final measurement at $P = 1700$ μW ($P = 20P_{sat}$), but this measurement could still be used. Between successive measurements, XY-scans were performed to check and compensate for possible drift and saturation measurements to ensure that I_∞ and P_{sat} remain unchanged.
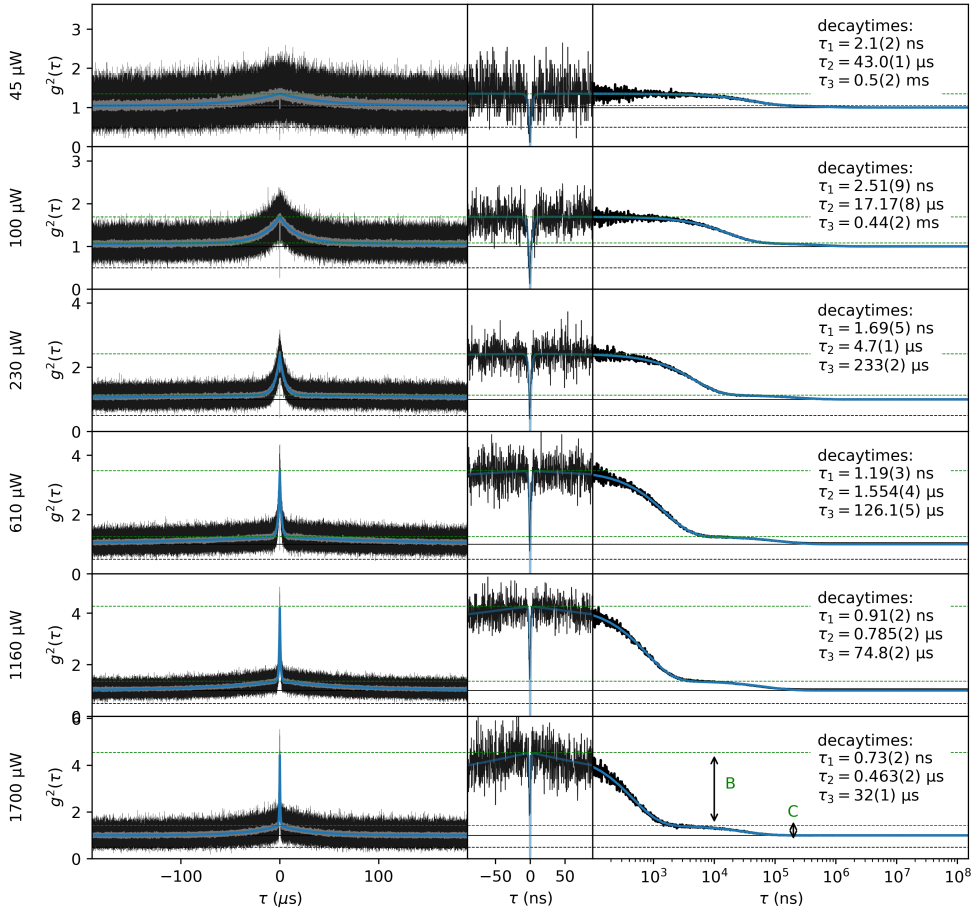

Figure 7.5: The second-order correlation function $g^2(\tau)$ measured for emitter B under continuous wave excitation for increasing excitation powers indicated on the left ($P_{sat} = 85$ μW). Figures from left to right show the same data for three ranges in time with bin sizes (from left to right) of 0.5 ns, 0.25 ns and exponentially increasing bin sizes. The gray curves on the left show the average of the black curves with a time window of 5 ns. All blue curves show the three-component fit from Eq. (7.1). The dashed green lines show the two bunching levels. A time-tagging mode instead of the standard start-stop method is used, in order to accurately determine these long time-scale decays.

Figure 7.6 shows the power dependence of the three fitted decay rates $s_i = 1/\tau_i$ and the

bunching amplitudes B and C. The fast rate s_1 has a zero-power offset and increases linearly with power as $s_1 = 0.43(3)$ ns^{-1}+49(3)P/P_{sat} μs^{-1}. The decay rates s_2 and s_3 go to zero at $P \approx 0$ and increase linearly with the power as $s_2 = 104(3)$ P/P_{sat} ms^{-1} and $s_3 = 1.53(4)$ P/P_{sat} ms^{-1}. Figure 7.6d shows the saturation curve, where $P_{\text{sat}} = 85(2)$ μW. The bunching amplitudes B and C in figures 7.6e and 7.6f are zero at $P \approx 0$ and increase strongly with power. This increase becomes less steep at higher powers. This observation is in contrast to observations by Boll et al. [127], where the bunching amplitude is approximately constant (see discussion below).
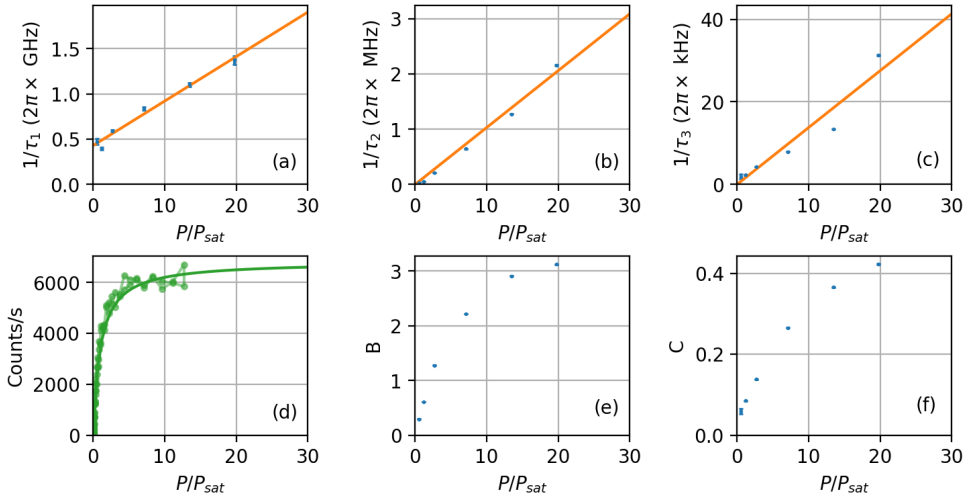

Figure 7.6: Parameters deduced from fits of $g^2(\tau)$, shown in Fig. 7.5, at various excitation powers: (a-c) decay rates s_1, s_2, s_3, (e-f) bunching amplitudes B and C for the rate s_2 and s_3 processes, respectively. (d) Observed count rate versus excitation power.

7.6. FOUR-LEVEL SYSTEM

The decay rates and bunching amplitudes shown in Fig. 7.6 can be modeled with a four-level system. Since the bunching rates s_2 and s_3 increase linearly with power, we expect some of the coupling rates in the four-level system to depend on power. We suggest two models to explain the observed dynamics: Model I (see also ref. [127]) and Model II. Note that in these models, we do not separate the decay k_{21} into a radiative and non-radiative decay, as done in ref. [126], since we cannot distinguish them experimentally. However, from the low observed count rates, we do expect the non-radiative decay rate to dominate.

The transition rates connecting the various levels can be computed using the measured decay rates s_1, s_2, s_3 and the bunching amplitudes B and C from Eq. (7.1). The complete analytical expressions for these variables are given in Appendix 7.A. For these computations, we assume a fixed $k_{21} = 0.43(3)$ ns^{-1}, derived from the $P \to 0$ limit in Fig. 7.6a.

Figures 7.8 and 7.9 show the calculated transition rates at different powers for Model I and Model II. All rates increase with power, often linearly but sometimes even quadrat-
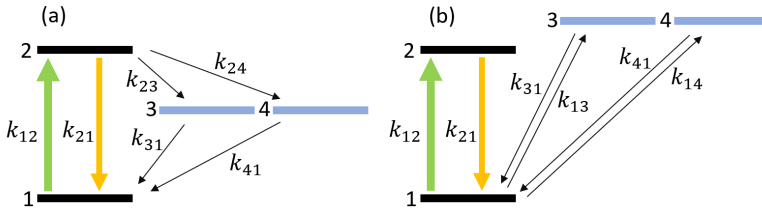
Figure 7.7: Two possible four-level systems to explain the observed dynamics: (a) Model I: the excitation laser only excites level 2 and the population of level 2 decays towards levels 3 and 4 with rates k_{23}, k_{24}. (b) Model II: The excitation laser excites all three levels 2, 3 and 4. Both models assume decay from levels 2, 3 and 4 to the ground state, level 1.

ically. In both models, the transition rates towards levels 3 and 4 (k_{23}, k_{24} for Model I and k_{13}, k_{14} for Model II) increase faster than the decay rates of levels 3 and 4 to the ground state (k_{31} and k_{41}). This causes "shelving" [128], meaning that for increasing powers the emitter is at the dark states for a larger portion of the time. Consequently, this should reduce the level-2 population, p_2, and the associated average count rate for increasing powers, as is shown in figure 7.8d. The measured emission, including a conventional saturation fit (see also figure 7.3b), is plotted on top of the calculated p_2. Comparing Figs. 7.8d and 7.9d, the measured (green points) and calculated (orange line) populations agree best for Model II, in figure 7.9. Note that both bunching amplitudes in Figs. 7.6e-f seem to saturation when $P \approx 9P_{sat}$ and $k_{12} \approx k_{21}$. We do not have a clear explanation for this at the moment and these observations might be coincidental.

The underlying physical mechanisms of the reported dynamics in the emitters remain unclear. Literature on hBN emitters with similar emission spectra do not always show the two bunching times that were observed here [119, 123]. Other studies that do show signs of two bunching times, either have a rather different emission spectrum [129], or their bunching dynamics depends differently on the power [127]. Some studies do report a very similar emission spectrum and bunching behavior in the auto-correlation function [121, 130], however, whether their origin is due to a spin ground state [121] or phonon-assisted excitation [38] remains unclear. It is therefore important to do a complete characterization of emitters, including polarization-dependent emission and excitation measurements [124], optically detected magnetic resonances [18], and multiple-color excitation measurements [131], to be able to thoroughly compare different reported measurements and theories.

7.7. CONCLUSION

In summary, several luminescent centers on a flake of hexagonal Boron Nitride were investigated. A colinear polarization scan was performed to select potential single-photon emitters. Two of those are stable for long times (> 10 hours at $P \sim P_{\text{sat}}$) such that they can be fully characterized. We find an optical spectrum with a peak around 580 nm and a phonon sideband around 640 nm. The polarization scan shows that the excitation dipole is better defined than the emission dipole. Furthermore, there is a shift of approximately 10 degrees between these dipole orientations. A measurement of the time dynamics of the
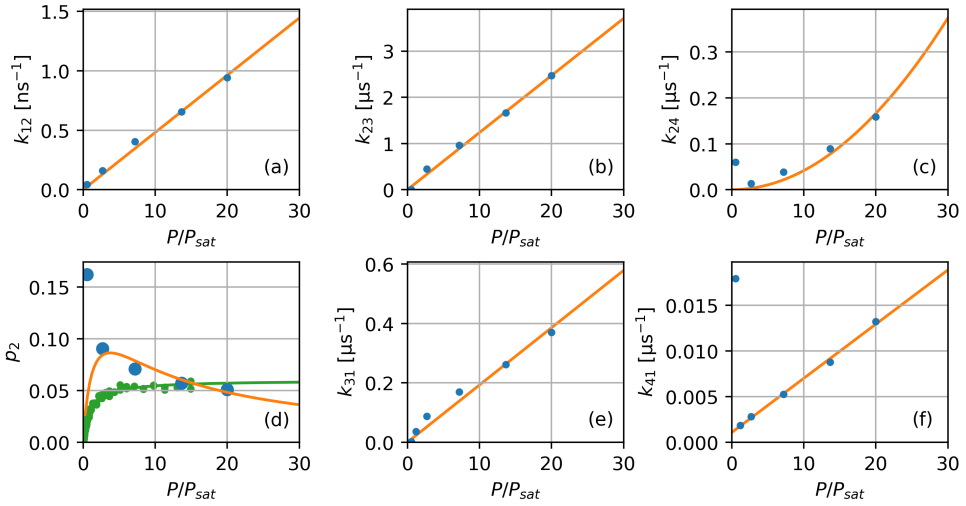
Figure 7.8: Decay rates of model I from figure 7.7a: (a-c) and (e-f) show all decay rates as a function of power (with fixed $k_{21} = 0.43(3)$ ns^{-1}). The fitted decay rates are: $k_{12} = 48(2)$ P/P_{sat} µs^{-1}, $k_{23} = 124(8)$ P/P_{sat} ms^{-1}, $k_{31} = 19.3(9)$ P/P_{sat} ms^{-1}, $k_{24} = 4.6(3)$ P/P_{sat} ms^{-1} + 0.27(3) $(P/P_{sat})^2$ ms^{-1} and $k_{41} = 1.1(2)$ ms^{-1} + 0.59(2) P/P_{sat} ms^{-1}. (d) Level-2 population: (blue) calculated based on the blue points in figures (a-c) and (e-f), (orange) calculated based on the orange fits in (a-c) to (e-f), (green) the measured steady-state emission rate, rescaled to better overlap with the orange curve.
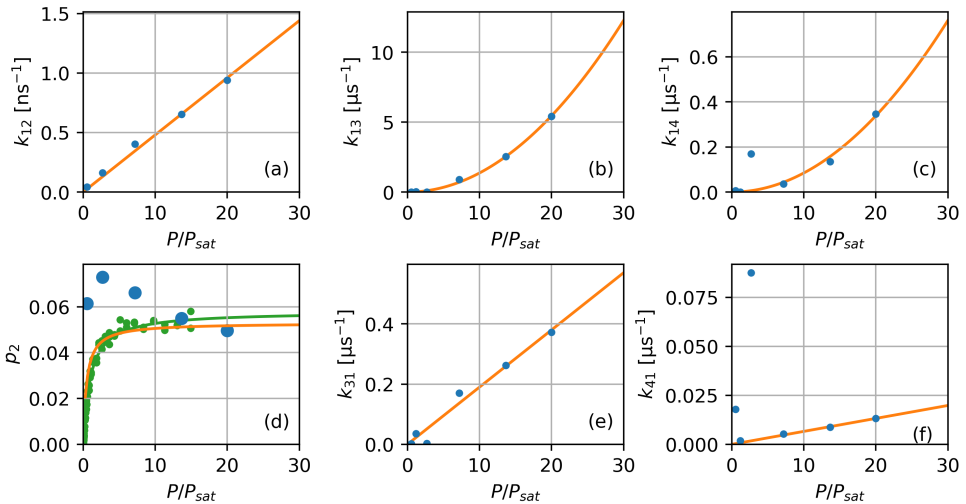

Figure 7.9: Decay rates of Model II from figure 7.7b: (a-c) and (e-f) show all decay rates as a function of power (with fixed $k_{21} = 0.43(3)$ ns^{-1}). The fitted decay rates are: $k_{12} = 48(2)$ P/P_{sat} µs^{-1}, $k_{13} = 13.6(2)$ $(P/P_{sat})^2$ ms^{-1}, $k_{31} = 19(1)$ P/P_{sat} ms^{-1}, $k_{14} = 0.8(2)$ $(P/P_{sat})^2$ ms^{-1} and $k_{41} = 0.66(2)$ P/P_{sat} ms^{-1}. (d) Level-2 population, (blue) calculated based on the blue points in figures (a-c) and (e-f), (orange) calculated based on the orange fits in (a-c) to (e-f), compared with (green) the directly measured steady-state emission, rescaled to better overlap with the orange curve.

singe-photon emission shows two distinct bunching processes with bunching times that differ by about one order of magnitude. Both bunching times decrease with increasing excitation power, while the amplitude of the bunching in the $g^2(\tau)$ measurements increases less quickly as the power increases. This behavior can be modeled with a four-level system with power-dependent decay rates. Our observations agree best with a model with three states that can be directly excited from the ground state. The quadratic power dependence of some of these rates suggests two-photon absorption processes.

Despite extensive study and several proposals [35, 36], the precise origin of hBN defects is still under discussion. The polarization shift between the dipoles and the dynamics of the two dark states that we observed in $g^2(\tau)$-measurements can be used to compare DFT studies with the measured emitters [50]. This comparison should result in a better understanding of these emitters in hBN.

7.8. ACKNOWLEDGMENTS

7.A. RATE EQUATIONS
In this appendix, we provide analytical solutions for the two different four-level systems that we introduced to explain the dynamics in figure 7.6 in the main text. The equations are inspired by ref. [126] and extend their solution for a three-level system to the four-level systems used here.

The equations describe the time-dependent level population p_i of the ith level, with transition rates k_{ij} for transitions from level i to level j. The total level population is 1 because it is a single-photon emitter. An analytical solution for the autocorrelation $g^2(\tau)$ is found, with expression for all parameters s_1, s_2, s_3, B and C from Eq. (7.1).

7.A.1. MODEL I, TWO DARK STATES
The rate equations for Model I are:

$$\begin{aligned}
\dot{p}_1 &= -k_{12}p_1 + k_{21}p_2 + k_{31}p_3 + k_{41}p_4 \\
\dot{p}_2 &= k_{12}p_1 - (k_{21} + k_{23} + k_{24})p_2 \\
\dot{p}_3 &= k_{23}p_2 - k_{31}p_3 \\
\dot{p}_4 &= k_{24}p_2 - k_{k41}p_4
\end{aligned} \tag{7.2}$$

with the constraint $1 = p_1 + p_2 + p_3 + p_4$ to set the total population to 1. This set of equations is overcomplete. If we write the ground-state population as $p_1 = 1 - p_2 - p_3 - p_4$, we obtain a system of three-coupled differential equations

$$\begin{pmatrix} \dot{p}_2 \\ \dot{p}_3 \\ \dot{p}_4 \end{pmatrix} + \begin{pmatrix} (k_{12} + k_{21} + k_{23} + k_{24}) & k_{12} & k_{12} \\ -k_{23} & k_{31} & 0 \\ -k_{24} & 0 & k_{41} \end{pmatrix} \begin{pmatrix} p_2 \\ p_3 \\ p_4 \end{pmatrix} = \begin{pmatrix} k_{12} \\ 0 \\ 0 \end{pmatrix}, \tag{7.3}$$

with the short-hand notation

$$\dot{\vec{p}} + \mathbf{M}\vec{p} = \vec{a}, \tag{7.4}$$

with $\vec{p} = (p_2, p_3, p_4)$ and $\vec{a} = (k_{12}, 0, 0)$.

We use the ansatz

$$\vec{p} = a\vec{A}e^{-s_1 t} + b\vec{B}e^{-s_2 t} + c\vec{C}e^{-s_3 t} + \vec{D}, \tag{7.5}$$

where $\vec{A}, \vec{B}, \vec{C}$ are the eigenvectors of the matrix $\mathbf{M}$, corresponding to their eigenvalues s_1, s_2, s_3, respectively and a, b and c are constants, determined by the boundary conditions.

The steady-state solution $\vec{D} = \mathbf{M}^{-1}\vec{a}$ is

$$\vec{D} = p_2^\infty \begin{pmatrix} 1 \\ k_{23}/k_{31} \\ k_{24}/k_{41} \end{pmatrix} \tag{7.6}$$

where

$$p_2^\infty = \left(1 + \frac{k_{23}}{k_{31}} + \frac{k_{24}}{k_{41}} + \frac{k_{21} + k_{23} + k_{24}}{k_{12}}\right)^{-1}. \tag{7.7}$$

The eigenvalues s_1, s_2, s_3 are the roots of the third-order polynomial equation

$$\frac{s - (k_{21} + k_{23} + k_{24})}{k_{12}} + \frac{k_{23}}{s - k_{31}} + \frac{k_{24}}{s - k_{41}} - 1 = 0 \tag{7.8}$$

with their corresponding eigenvectors

$$\vec{A}, \vec{B}, \vec{C} = \frac{1}{\sqrt{1 + \left(\frac{k_{23}}{s - k_{31}}\right)^2 + \left(\frac{k_{24}}{s - k_{41}}\right)^2}} \begin{pmatrix} 1 \\ -\frac{k_{23}}{s - k_{31}} \\ -\frac{k_{24}}{s - k_{41}} \end{pmatrix} \tag{7.9}$$

where $s = s_1, s_2, s_3$ for eigenvectors $\vec{A}, \vec{B}, \vec{C}$, respectively.

The autocorrelation function $g_2(\tau) = \frac{p_2(\tau)}{p_2^\infty}$ is the solution for the time-dependent population p_2 with the initial condition that a photon has just been emitted, $p_1(\tau = 0) = 1$, and thus $\vec{p} = \vec{0}$. With this initial condition, the constants in Eq. (7.5) are $a = -\vec{A} \cdot \vec{D}$, $b = -\vec{B} \cdot \vec{D}$ and $c = -\vec{C} \cdot \vec{D}$. The bunching amplitude in Eq. (7.1) can thus be expressed as $B = \frac{-\vec{B} \cdot \vec{D}}{p_2^\infty}\vec{B}[0]$ and $C = \frac{-\vec{C} \cdot \vec{D}}{p_2^\infty}\vec{C}[0]$, where $\vec{B}[0]$ and $\vec{C}[0]$ are the first elements of the eigenvectors. The explicit solution to the bunching amplitudes are

$$B, C = -\frac{1 - \frac{k_{23}^2}{k_{31}(s - k_{31})} - \frac{k_{24}^2}{k_{41}(s - k_{41})}}{1 + \left(\frac{k_{23}}{s - k_{31}}\right)^2 + \left(\frac{k_{24}}{s - k_{41}}\right)^2} \tag{7.10}$$

where $s = s_2$ and $s = s_3$ for amplitudes B and C respectively.

7.A.2. MODEL II, EXCITATION TOWARDS TWO HIGHER LEVELS
This model is solved in the same way, but has slightly different rate equations:

$$\begin{aligned}
\dot{p}_1 &= -(k_{12} + k_{13} + k_{14})p_1 + k_{21}p_2 + k_{31}p_3 + k_{41}p_4, \\
\dot{p}_2 &= k_{12}p_1 - k_{21}p_2, \\
\dot{p}_3 &= k_{13}p_1 - k_{31}p_3, \\
\dot{p}_4 &= k_{14}p_1 - k_{k41}p_4
\end{aligned} \tag{7.11}$$

with the constraint $1 = p_1 + p_2 + p_3 + p_4$ to set the total population to 1.

In the matrix form, the three-coupled different equations are

$$\begin{pmatrix} \dot{p}_2 \\ \dot{p}_3 \\ \dot{p}_4 \end{pmatrix} + \begin{pmatrix} (k_{12} + k_{21}) & k_{12} & k_{12} \\ k_{13} & (k_{31} + k_{13}) & k_{13} \\ k_{14} & k_{14} & (k_{41} + k_{14}) \end{pmatrix} \begin{pmatrix} p_2 \\ p_3 \\ p_4 \end{pmatrix} = \begin{pmatrix} k_{12} \\ k_{13} \\ k_{14,} \end{pmatrix} \tag{7.12}$$

with short-hand notation

$$\dot{\vec{p}} + \mathbf{M}\vec{p} = \vec{a} \tag{7.13}$$

where $\vec{a} = (k_{12}, k_{13}, k_{14})$.

The same ansatz is made,

$$\vec{p} = a\vec{A}e^{-s_1 t} + b\vec{B}e^{-s_2 t} + c\vec{C}e^{-s_3 t} + \vec{D}, \tag{7.14}$$

with steady-state solution

$$\vec{D} = \frac{k_{21}}{k_{12}} p_2^\infty \begin{pmatrix} k_{12}/k_{21} \\ k_{13}/k_{31} \\ k_{14}/k_{41} \end{pmatrix} \tag{7.15}$$

where

$$p_2^\infty = \frac{k_{12}}{k_{21}} \left(1 + \frac{k_{12}}{k_{21}} + \frac{k_{13}}{k_{31}} + \frac{k_{14}}{k_{41}} \right)^{-1}. \tag{7.16}$$

The eigenvalues s_1, s_2, s_3 are now given by

$$\frac{k_{12}}{s - k_{21}} + \frac{k_{13}}{s - k_{31}} + \frac{k_{14}}{s - k_{41}} - 1 = 0 \tag{7.17}$$

with eigenvectors

$$\vec{A}, \vec{B}, \vec{C} = \frac{1}{\sqrt{\left(\frac{k_{12}}{s-k_{21}}\right)^2 + \left(\frac{k_{13}}{s-k_{31}}\right)^2 + \left(\frac{k_{14}}{s-k_{41}}\right)^2}} \begin{pmatrix} \frac{k_{12}}{s-k_{21}} \\ \frac{k_{13}}{s-k_{31}} \\ \frac{k_{14}}{s-k_{41}} \end{pmatrix} \tag{7.18}$$

The bunching amplitudes form Eq. (7.1) for model II are,

$$B, C = -\frac{k_{21}}{s - k_{21}} \frac{\frac{k_{12}^2}{k_{21}(s-k_{21})} + \frac{k_{13}^2}{k_{31}(s-k_{31})} + \frac{k_{14}^2}{k_{41}(s+k_{41})}}{\left(\frac{k_{12}}{s-k_{21}}\right)^2 + \left(\frac{k_{13}}{s-k_{31}}\right)^2 + \left(\frac{k_{14}}{s-k_{41}}\right)^2} \tag{7.19}$$

where $s = s_2$ for B and $s = s_3$ for C.

7.B. TRANSITION RATES OF EMITTER A

This Appendix described the measurements and analyses of the dynamics of emitter A, to be compared with emitter B in the main text. Figure 7.10 shows the measured auto-correlation functions of emitter A at three different powers, where the saturation power is $P_{\text{sat}} = 74(2)\ \mu$W. Similar to emitter B, there are clearly two bunching time scales that differ by more than an order of magnitude.

Figure 7.11 shows the fitted transition rates and bunching amplitudes. The decay rates scale linearly with the power with fitted rates $s_1 = 0.35$ ns^{-1} + 63(7) P/P_{sat} μs^{-1}, $s_2 = 67(5)$ P/P_{sat} ms^{-1} and $s_3 = 1.5(3)$ P/P_{sat} ms^{-1}. The figure shows behavior that is both qualitatively and quantitatively similar to figure 7.6. This indicates that the dynamics of emitter A and B are determined by the same process.
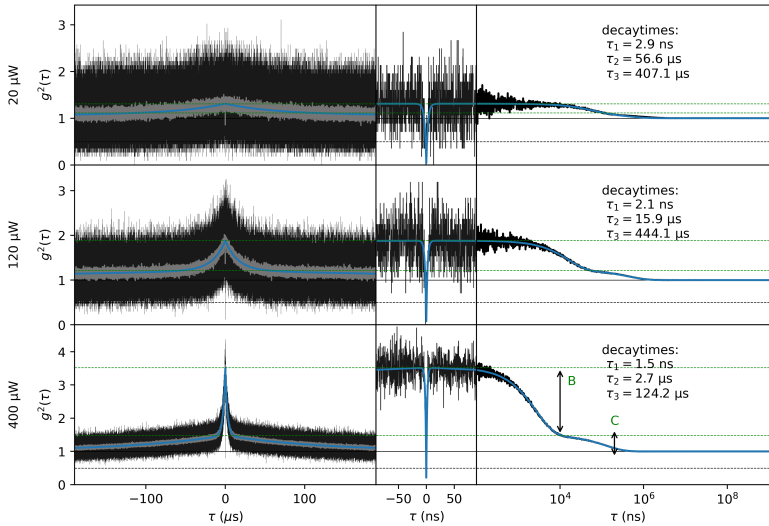

Figure 7.10: The second-order correlation function $g^2(\tau)$ measured for emitter A under continuous wave excitation for increasing excitation powers ($P_{sat} = 74$ μW).
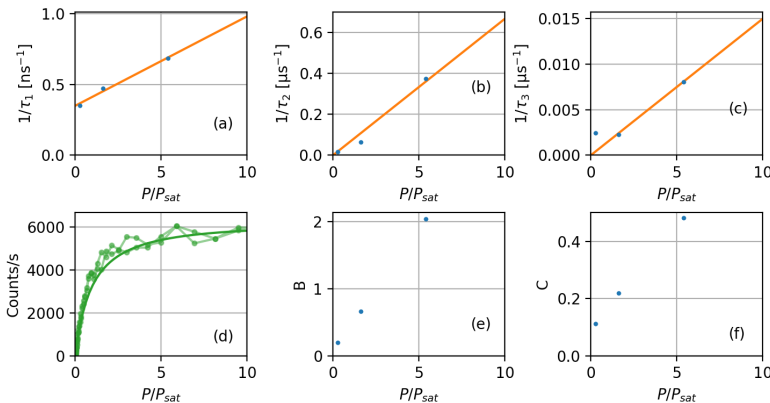

Figure 7.11: Parameters deduced from fits of $g^2(\tau)$ shown in Fig. 7.10, at three excitation powers: (a-c) decay rates s_1, s_2, s_3, (e-f) bunching amplitudes B and C for the rate s_2 and s_3 processes, respectively. (d) Observed count rate versus excitation power.

7.C. MEASUREMENTS ON EMITTER C

This appendix describes measurements on the almost stable emitters. These bleach relatively quickly, between half an hour to 2 hours at $P \sim P_{\text{sat}}$. We find several such emitters, but a full characterization is challenging due to their fast bleaching times. The emitter shown here, emitter C, bleached after about 3 hours, such that most measurements could be completed.

Figs. 7.12, 7.13 and 7.14 show three experiments where emitter C differs from emitters A and B. First, at saturation (see figure 7.12), its count rate is 33.0(7) kCounts/s, which is about a factor 5 larger than the count rates observed for emitters A and B. Also the saturation power of emitter C, $P_{\text{sat}} = 147(6)$ μW, is about a factor 2 larger than that of emitters A ($P_{\text{sat}} = 74(2)$ μW) and B ($P_{\text{sat}} = 85(2)$ μW). Furthermore, a linearly increasing background fluorescence of 1.9(4) counts/μW is required to properly fit the saturation curve. Second, the measurement of the angle-dependent excitation and emission in figure 7.13 shows no difference in dipole orientation within error margins of 2 degrees. This is also in contrast to emitters A and B, where the difference was about 10 degrees. Third, the autocorrelation function $g^2(\tau)$ in figure 7.14 shows only one clear bunching time scale, instead of two as was measured for emitters A and B.

The flakes contain more emitters that are similar to emitter C. Despite their brightness being larger, the faster bleaching of such emitters makes them less useful for applications.
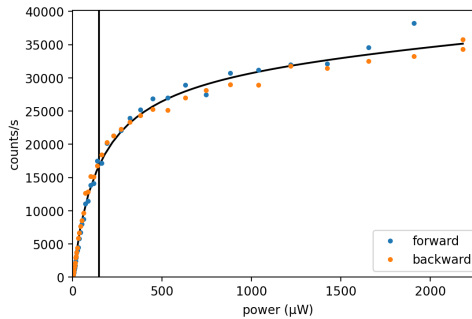

Figure 7.12: Saturation curve measured for emitter C. The blue/orange points are measured upon increase/decrease of the excitation power.
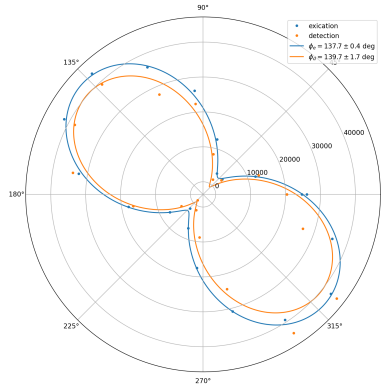
Figure 7.13: Polarization plot of the excitation and emission dipoles for emitter C. Both curves are fitted with a $\cos(\theta)^2$-relation with an offset.
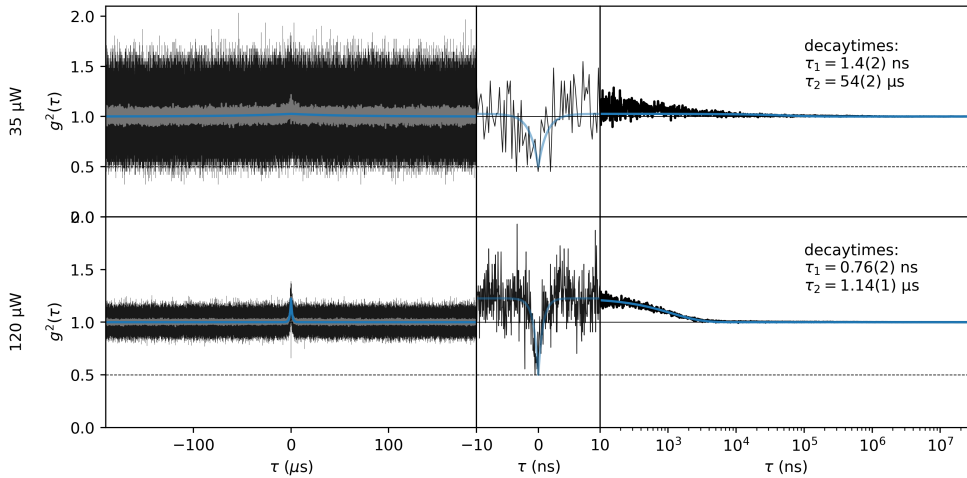

Figure 7.14: The second order autocorrelation function $g^2(\tau)$ of emitter C for two different powers. The dip is set to 1/2 instead of 0, because this emitter is most likely not a single-photon emitter.